Electronic Supplementary Material (ESI) for Energy & Environmental Science.

Electronic Supplementary Information

Triboelectric Nanogenerators: Providing a Fundamental Framework

R.D.I.G. Dharmasena[a], K.D.G.I. Jayawardena[a], C.A. Mills[a,b], J.H.B. Deane[c], J.V. Anguita[a], R.A. Dorey[d], S.R.P. Silva[a]*

[a] *Advanced Technology Institute, Department of Electrical and Electronic Engineering, University of Surrey, Guildford, Surrey, GU2 7XH, United Kingdom. Email: s.silva@surrey.ac.uk*

[b] *Advanced Coatings Group, Tata Steel Research Development and Technology, Voyager Building 9, Sir William Lyon Road, Coventry CV4 7EZ, United Kingdom*

[c] *Department of Mathematics, University of Surrey, Guildford, Surrey, GU2 7XH, United Kingdom.*

[d] *Centre for Engineering Materials, Mechanical Engineering Sciences, University of Surrey, Guildford, Surrey, GU2 7XH, United Kingdom.*

Contents:

Supplementary Note 1: Derivation of the distance-dependent electric field equation

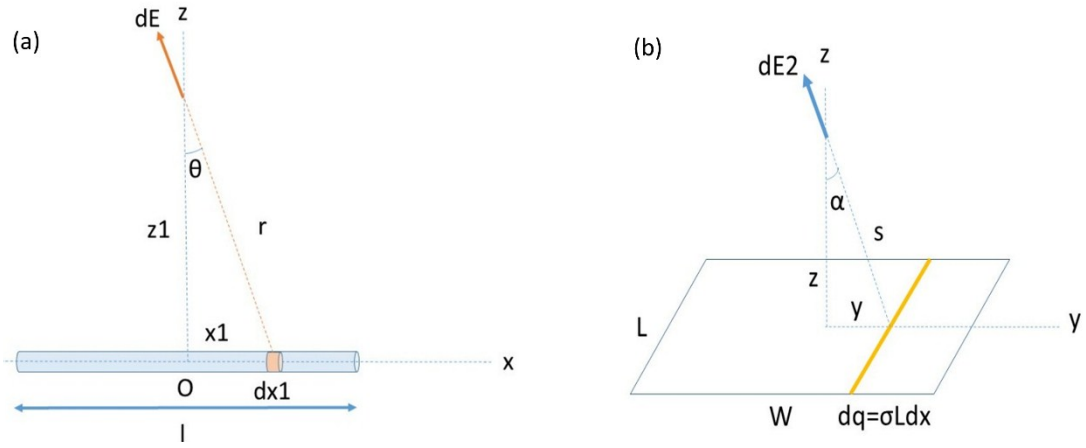

Fig. S.1: Derivation of the electric field equations along a perpendicular axis, above the mid-point of a uniformly charged (a) line, and, (b) a sheet.

Consider a line of length l, with a uniform linear charge density σ_1. The electric field variation above the midpoint of the line along z axis can be derived as follows (Fig. S.1a);

The charge on the small line segment (dx1) = $\sigma_1 dx1$ (S1)

The contribution to the electric field resulting from the line segment $dE = \frac{1}{4\pi\varepsilon_0} \frac{\sigma_1 dx1}{(x1^2 + z^2)}$ (S2)

Hence, the component of electric field along z axis $dE_z = dE cos\theta = \frac{1}{4\pi\varepsilon_0} \frac{\sigma_1 dx1}{(x1^2 + z^2)^{3/2}}$ (S3)

Considering symmetry and integrating along the length of the line,

$$E_z = \int dE_z = \frac{\sigma_1}{4\pi\varepsilon_0 z} \frac{l}{[(l/2)^2 + z^2]^{1/2}} \quad \text{(S4)}$$

Similarly, a uniformly charged plane with a surface charge density of σ is composed of a collection of lines along the y axis (Fig. S.1b). The overall electric field above the midpoint along the z axis,

$$dE_{z,plane} = dE_z cos\alpha \quad \text{(S5)}$$

Integrating along the y axis and simplifying,

$$E_{z,plane} = \frac{\sigma}{\pi\varepsilon_0} \arctan\left[\frac{\frac{L}{W}}{2\left(\frac{Z}{W}\right)\sqrt{4\left(\frac{Z}{W}\right)^2 + \left(\frac{L}{W}\right)^2 + 1}}\right] = \frac{\sigma}{\pi\varepsilon_0} f(z) \quad \text{(S6)}$$

$$f(z) = \arctan\left[\frac{\frac{L}{W}}{2\left(\frac{Z}{W}\right)\sqrt{4\left(\frac{Z}{W}\right)^2 + \left(\frac{L}{W}\right)^2 + 1}}\right]$$

where,

Supplementary Note 2: Evaluating the inverse tangent (arctan) integral

Let us look at the integral of the arctan function. Define,

$$M(x) = \int \arctan\left(\frac{\frac{L}{W}}{2\left(\frac{x}{W}\right)\sqrt{4\left(\frac{x}{W}\right)^2 + \left(\frac{L}{W}\right)^2 + 1}}\right)dx = \int f(x)dx \tag{S7}$$

When $L = W$ this can be evaluated in closed form. Eqn (S7) then becomes,

$$M(x) = \int \arctan\left(\frac{1}{2\left(\frac{x}{W}\right)\sqrt{4\left(\frac{x}{W}\right)^2 + 2}}\right)dx = \int 1 * \arctan\left(\frac{1}{2\left(\frac{x}{W}\right)\sqrt{4\left(\frac{x}{W}\right)^2 + 2}}\right)dx \tag{S8}$$

Integrating by parts,

$$M(x) = x\arctan\left(\frac{W}{2x\sqrt{\frac{4x^2}{W^2} + 2}}\right) - Warctanh\sqrt{\frac{4x^2}{W^2} + 2} + C$$

, where C is a constant (S9)

x represents the thickness of the TENG layers and the separation between them, hance $x > 0$. This implies

$$\forall x,\ \sqrt{\frac{4x^2}{W^2} + 2} \geq \sqrt{2} > 1 \tag{S10}$$

$\text{arctanh}\,(x),\ x > 1$ is complex. Therefore, $M(x)$ contains a complex componant. Let us further analyze the $arctanh$ (inverse hyperbolic tangent) function.

Define $$y = arctanh\sqrt{\frac{4x^2}{W^2} + 2}$$

Rearranging the function [1],

$$\text{arctanh}\,(y) = \frac{1}{2} ln\left(\frac{1+y}{1-y}\right)$$

Using Euler's identity [1], $e^{i\pi} = -1$

$$\text{arctanh}\,(y) = \frac{1}{2} ln\left[e^{i\pi}\left(\frac{1+y}{y-1}\right)\right] = \frac{i\pi}{2} + \frac{1}{2} ln\left(\frac{y+1}{y-1}\right) \tag{S11}$$

From eqn (S10), $\forall x, \frac{1}{2} ln\left(\frac{y+1}{y-1}\right)$ is a real value. Furthermore, the integral is evaluated between positive limits a and b.

$$\text{arctanh}\,(y)|_b^a = \frac{1}{2}\ln\left(\frac{a+1}{a-1}\right) - \frac{1}{2} ln\left(\frac{b+1}{b-1}\right)$$

and $\frac{i\pi}{2}$ dissappears. Hence,

$$[M(x)]_b^a = \left[x\arctan\left(\frac{W}{2x\sqrt{\frac{4x^2}{W^2}+2}}\right) - \frac{W}{2} ln\left(\frac{\sqrt{\frac{4x^2}{W^2}+2}+1}{\sqrt{\frac{4x^2}{W^2}+2}-1}\right) \right]_b^a \tag{S12}$$

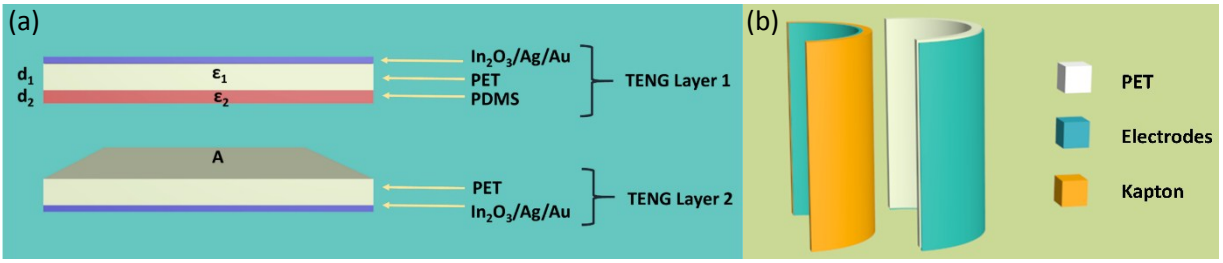

Supplementary Note 3: TENG architectures

Fig. S.2: The architecture of (a) the planar TENG device, and, (b) the non-planar (curved) TENG device.

Planar TENG device (Fig. S.2a)

Thickness of the PET layer (d_1) = 200 µm

Thickness of the PDMS layer (d_2) = 20 µm

Permittivity of free space = ε_0

Permittivity of PET (ε_1) = $3.3\varepsilon_0$

Permittivity of PDMS (ε_2) = $2.72\varepsilon_0$

The overall permittivity for the PET/PDMS combined layer of TENG layer 1 can be approximated as

$$C = \frac{\varepsilon A}{d} \tag{S13}$$

where C is the capacitance, ε is the permittivity and d is the thickness of the dielectric layer.

Using parallel plate capacitor model,

$$\frac{1}{C_T} = \frac{1}{C_1} + \frac{1}{C_2} \tag{S14}$$

Where C_1, C_2 and C_T indicates the capacitance of the PET layer, PDMS layer, and the total capacitance of TENG layer 1 respectively.

$$\varepsilon_T = \frac{\varepsilon_1 \varepsilon_2 (d_1 + d_2)}{d_1 \varepsilon_2 + d_2 \varepsilon_1} \tag{S15}$$

Substituting $\varepsilon_1 = 3.3\varepsilon_0, \varepsilon_2 = 2.72\varepsilon_0, d1 = 0.2\ mm\ and\ d2 = 0.02\ mm$,

$$\varepsilon_T \sim 3.24\varepsilon_0$$

Hence,

Permittivity of TENG layer 1 = 3.24^{ε_0}

Permittivity of TENG layer 2 = 3.3^{ε_0}

Non-planar (curved) TENG device (Fig. S.2b)

A non-planar TENG device was fabricated using a PET sheet (as the previous device) and a Kapton sheet (thickness 0.05 mm, DuPont (USA)) as TENG contact surfaces (Fig. S.2b). An aluminium layer (thickness 120 nm) was deposited on the back side of the Kapton sheet, which acted as an electrode. The selection of the materials for the non-planar device was based on the convenience of fabrication along curved surfaces. Two hollow semi-cylindrical holders were constructed, one with the outer diameter of 32 mm (for the convex surface) and the other with inner diameter of 32 mm (concave surface), both with a length (L) of 50 mm. A 50 mm $\times$ 50 mm PET layer was attached to the concave surface and a Kapton sheet with similar area was attached to the convex surface.

Permittivity of Kapton layer = $^{3.5\varepsilon_0}$

Figure S.3: Contact and separation apparatus

(a)

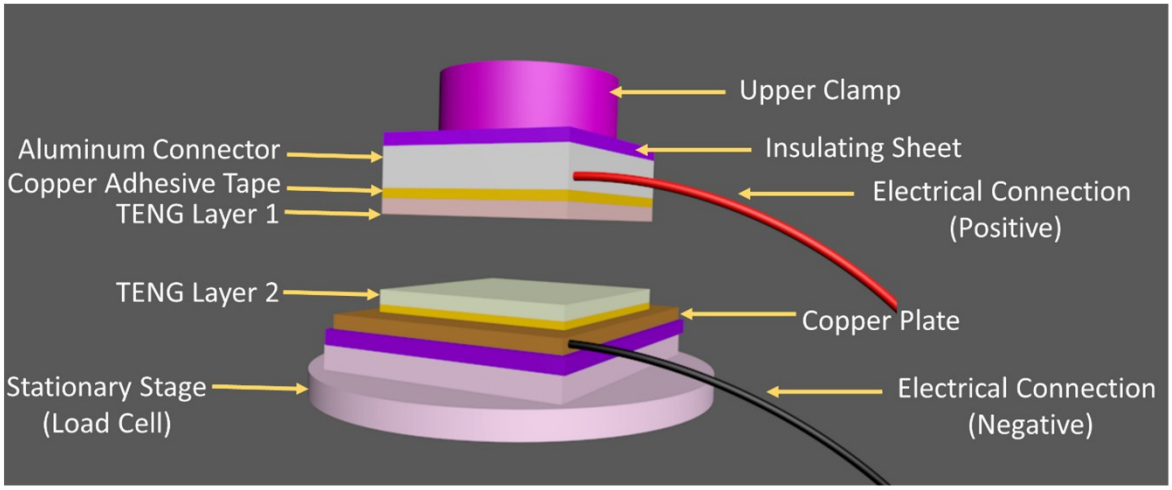

(b)

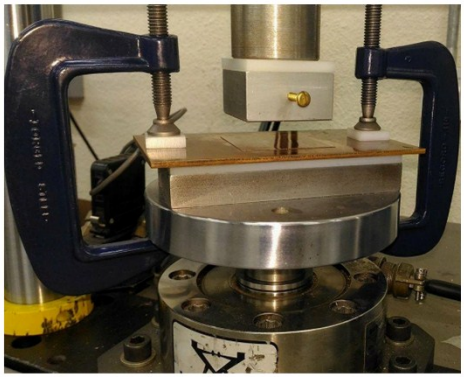

Fig. S.3: (a) A schematic representation, and, (b) a photograph, of the Instron 8511 contact and separation apparatus with the modifications.

The apparatus used for contact-separation movement of the planar TENG layers is a modified Instron 8511 fatigue testing system. TENG layers were attached to metal holders (Aluminium connector and copper plate) using conductive tapes, and these holders were electrically isolated from the rest of the setup using two insulating sheets. The PDMS coated layer (TENG layer 1) was connected to the upper clamp whereas the PET sheet (TENG layer 2) was connected to the opposite, stationary stage.

The positive lead of the electrometer/picoammeter was connected to the metal holder which held the PDMS coated layer, and the negative lead was connected to the copper plate holding the PET layer. The displacement at which the upper clamp applied 20 N force on the stationary stage (load cell), was considered as the reference contact position for the TENG sheets ($z = 0$), and the separation of the sheets was measured relative to this position.

Given the relative position of PDMS and PET in the triboelectric series, PDMS charges negatively, and PET positively.[2] Hence, during the contact half cycle a positive current peak and a positive output charge flow were recorded. The sign of the current and output charge reversed during the separation half cycle. Furthermore, the sign of the measured voltage was negative when the TENG layers were separated from contact position, and positive during the contact movement.

A custom-made high-precision motion control system operated via a linear motor was used to execute the movements of the non-planar TENG device. Conductive tapes were used to attach the TENG layers to the curved holders. Positive lead of the measurement units was connected to the PET layer and the

negative, to the Kapton layer. The same test procedure which was used for the planar TENG device was used to test the non-planar device.

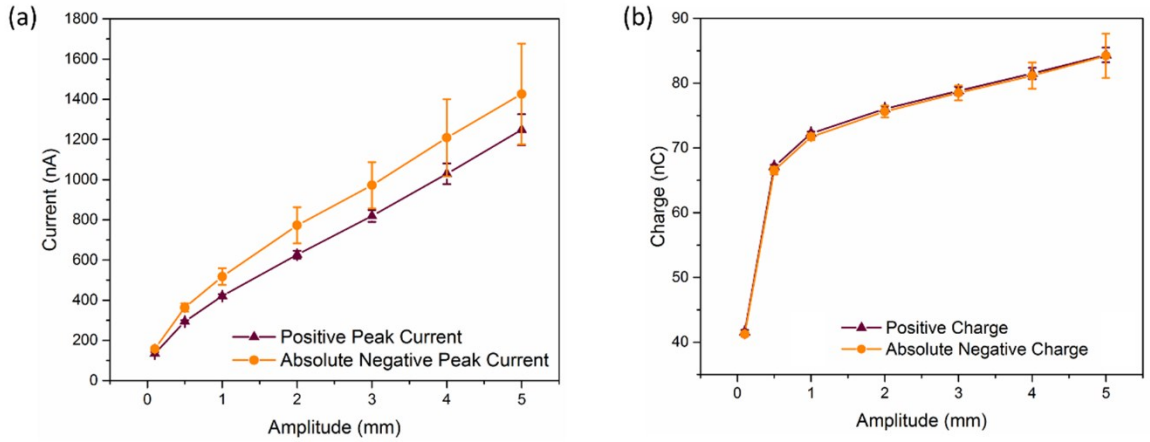

Fig. S.4: Comparison of magnitudes of the short circuit current output during amplitude variation at f =1 Hz. (a) peak current, and, (b) output charge, during positive and negative output cycles; Error bars indicate standard deviation of 30 readings.

Figure S.4: Comparison of peak current and output charge during variation of amplitude

Figure S.5: Comparison of peak current and charge during variation of frequency

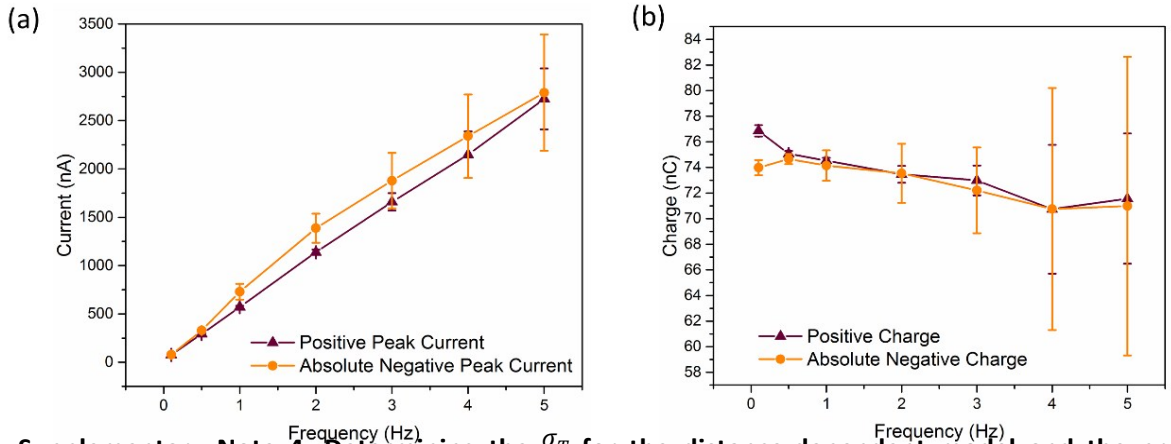

Fig. S.5: Comparison of the magnitudes of short circuit current output during frequency variation at H=1 mm. (a) peak current, and, (b) output charge, during positive and negative output cycles; Error bars indicate standard deviation of 30 readings.

Supplementary Note 4: Determining the σ_T for the distance-dependent model and the previously published model

Current and output charge measurements in the short circuit condition against different frequencies and amplitudes were used as a key parameter in the characterization of the TENG structure. The experimental current and output charge values (depicted in Fig. 2b-e of the main text) were compared with the corresponding predictions from the models, and the least squares method was used to determine the σ_T which minimizes the summation of the squared percentage error.

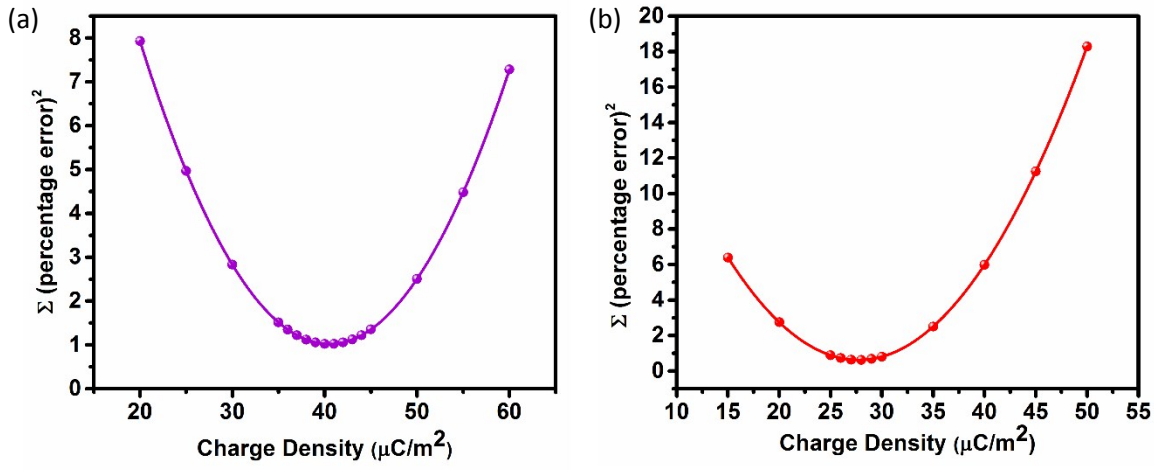

Fig. S.6: Sum of the squared percentage error of open circuit output charge and current, between the experimental and the (a) distance-dependent model, and, (b) previously published model[3].

The minimum overall error was achieved at σ_T=40.7 for the distance-dependent model, and σ_T=27.6 for the previously published model[3]. These values were then used for corresponding voltage and power predictions during the study.

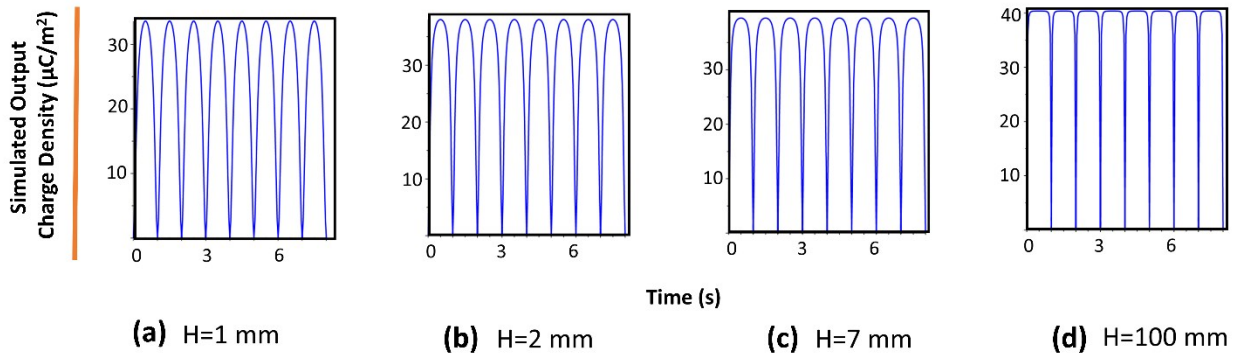

Figure S.7: Dependence of σ_U on the amplitude of movement (H), for a given σ_T

Fig. S.7: The simulated behaviour of the output charge density using the distance-dependent model, when R=10 Ω, f=1 Hz, and at increasing H. (a) H=1 mm, (b) H=2 mm, (c) H=7 mm, and, (d) H=100 mm.

Figure S.8: **Comparison of the experimental results and the predictions from the previously published**

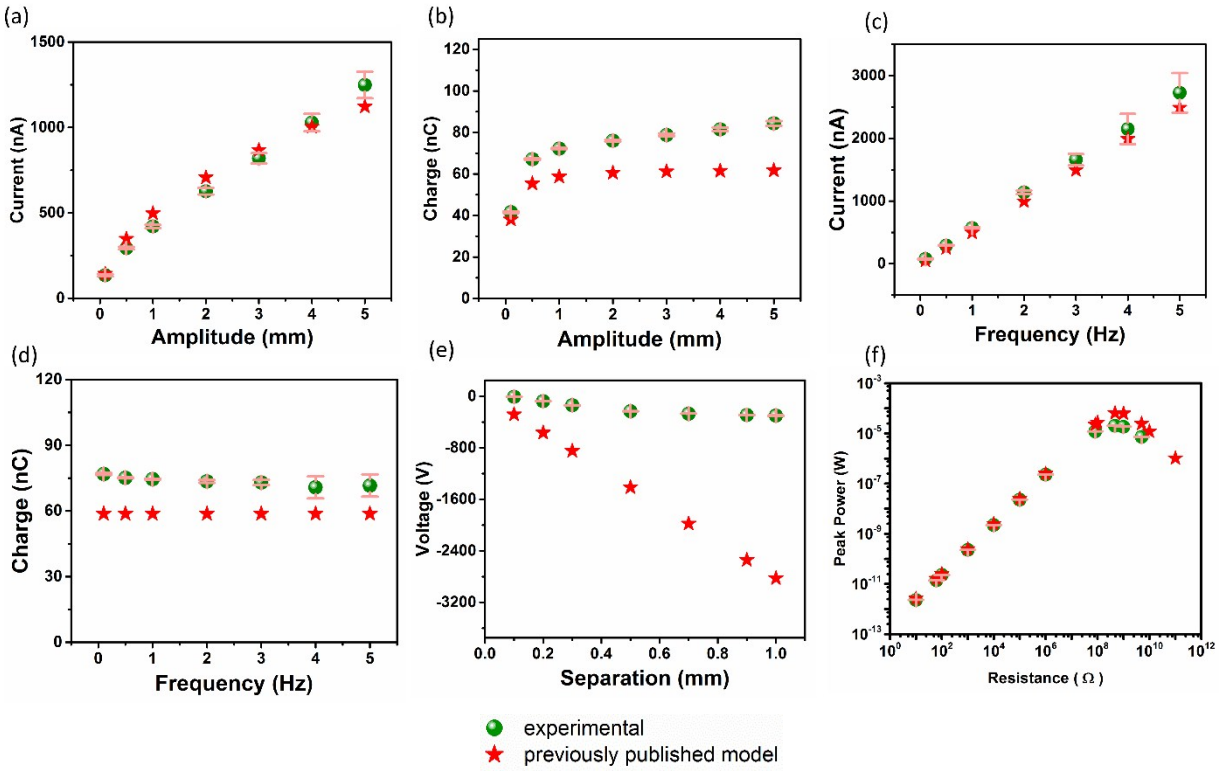

Fig. S.8: Comparison of experimental outputs with the predictions from the previously published model. Short circuit (a) peak current, and, (b) accumulated charge at f=1 Hz and different H values. Short circuit (c) peak current, and, (d) accumulated charge at H= 1 mm and different f values. Comparison of (e) V_{OC} at different separations of TENG layers, and, (f) peak power output through different resistors when H=1 mm and f=1 Hz; Error bars indicate standard deviation of 30 readings.

model[3], at an assumed σ_T of 27.6 μC/m².

Figure S.9: Comparison of the experimental results, with the predictions from the previously published model[3] and the distance-dependent model, at an assumed σ_T of 48 μC/m².

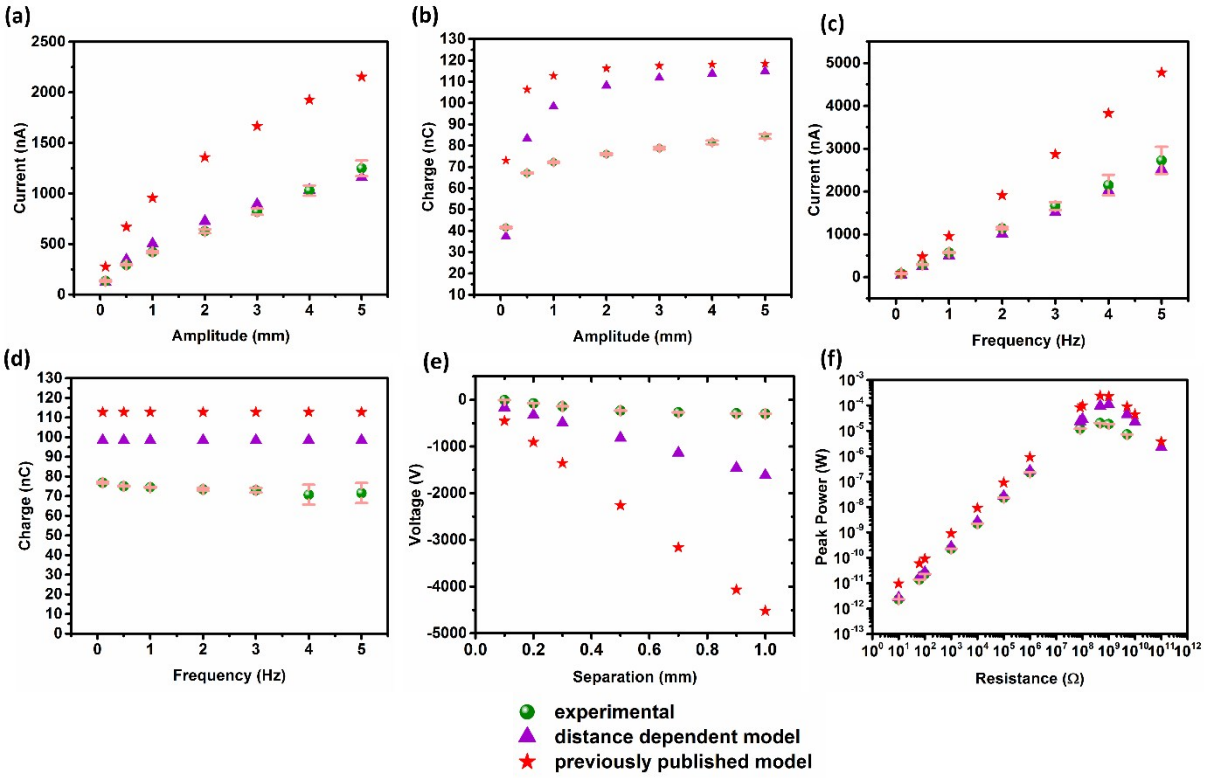

Fig. S.9: Comparison of experimental outputs with the predictions from the models. Short circuit (a) peak current, and, (b) accumulated charge at f=1 Hz and different H values. Short circuit (c) peak current, and, (d) accumulated charge at H= 1 mm and different f values. Comparison of (e) V_{OC} at different separations of TENG layers, and, (f) peak power output through different resistors when H=1 mm and f=1 Hz; The charge density for both the models is 48 μC/m². Error bars indicate standard deviation of 30 readings.

Supplementary Note 5: The spatial variation of the electric field originating from triboelectrically charged surfaces

The electric field orignating from finitely large charged surfaces decay with the increasing distance from the surface. Electric field variation aginst the distance from a positively charged surface is modelled using eqn (2) (Fig. S.10a), and the overall electric field resulting from two oppositely charged surfaces (Fig. 1c) against the separation of sheets (z) is modelled using eqn (5) (Fig. S.10b). For comparison purposes, the electric field is asusmed to propogate in free space, with the permttivity of free space used for both S.10a and S.10b. The parameters of the equations are assumed as follows,

$L = W = 0.05\ m$, $\varepsilon_1 = \varepsilon_0 = 8.85418 \times 10^{-12}\ m^{-3} kg^{-1} s^4 A^2$, $\sigma_T = 48\ \mu C/m^2$, and $x_1 = 0.0002\ m$

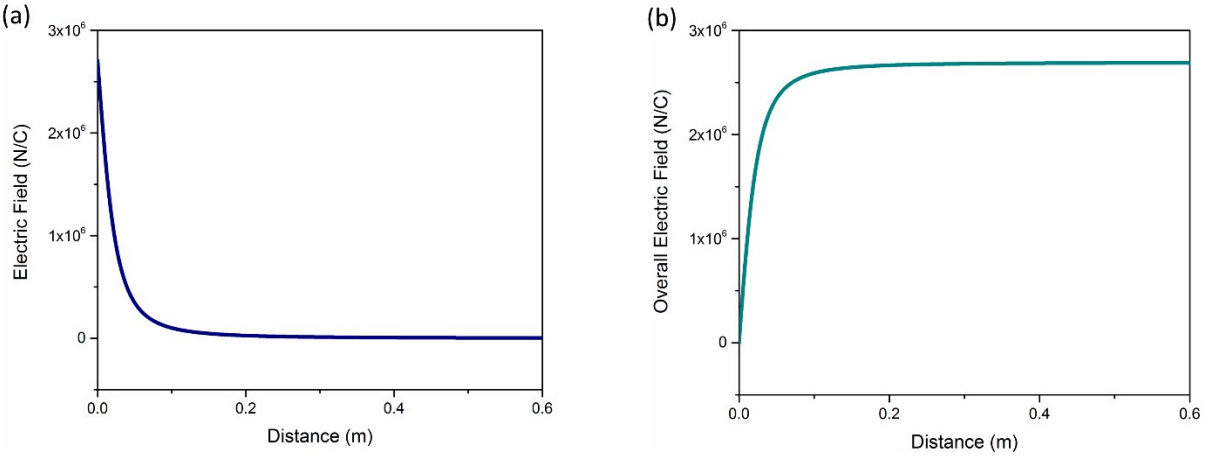

Fig. S.10: The electric field variations against distance. (a) The electric field originating from a finitely large charged sheet (as shown in Fig. S.1b), plotted against the distance from the charged surface, and, (b) the overall electric field on the dielectric-electrode interface of a TENG resulting from oppositely charged sheets (as shown in Fig. 1c), plotted against the separation of the charged surfaces.

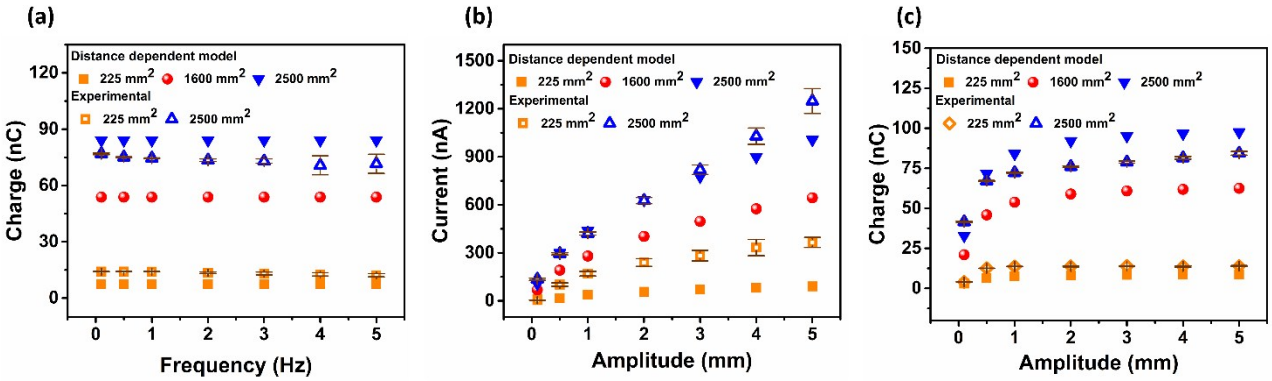

Fig. S.11: Comparison of experimental (hollow markers) and simulated TENG outputs using the distance-dependent model (solid markers) for the short circuit condition, indicting (a) output charge against increasing f (at H=1 mm), and, (b) peak current and (c) output charge against increasing H (f=1 Hz), for different TENG contact surface areas. Error bars indicate the standard deviation of 10 readings.

Figure S.11: Variation of current and charge output against different contact surface areas

Figure S.12: Variation of current and charge output against different PDMS layer thicknesses

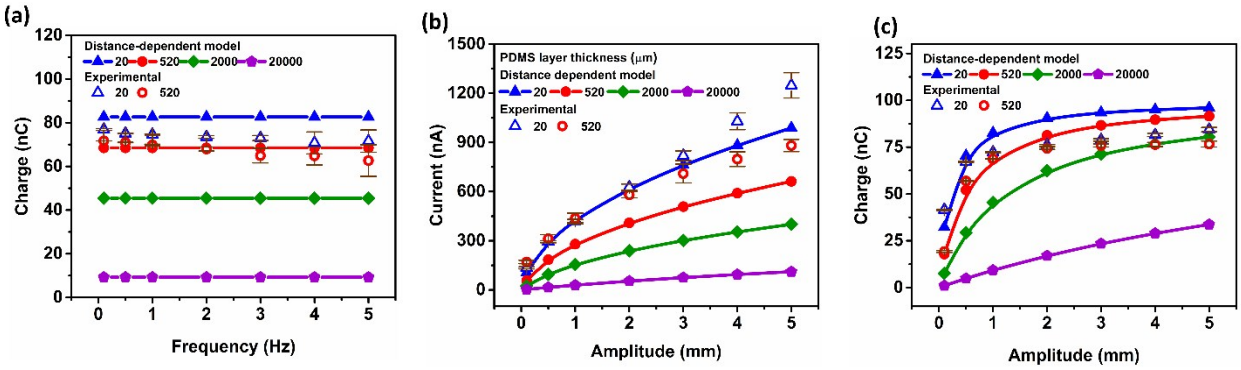

Fig. S.12: Comparison of experimental (hollow markers) and simulated TENG outputs using the distance-dependent model (solid markers) for the short circuit condition, indicting (a) output charge against increasing f (at H=1 mm), and, (b) peak current and (c) output charge against increasing H (f=1 Hz), for different PDMS layer thicknesses. Error bars indicate the standard deviation of 10 readings.

Supplementary Note 6: Derivation of the overall electric fields for curved surfaces

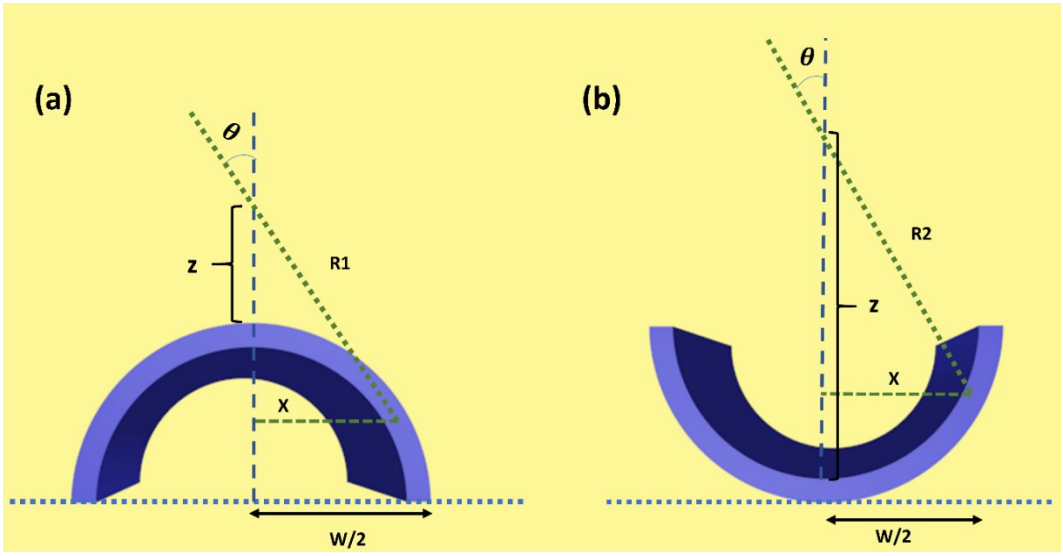

Fig. S.13: Deriving the overall electric field equations for the (a) convex, and, (b) concave TENG surfaces.

Using similar methods described in supplementary note 1 for the convex surface, overall electric field over the midpoint of the surface along z axis,

$$E_{z,convex} = \frac{\sigma L}{\pi\varepsilon_0}\int_0^{w/2} \frac{(z+\frac{w}{2}-\sqrt{\frac{w^2}{4}-x^2})}{{R_1}^2\sqrt{4{R_1}^2+L^2}}dx \quad \text{, where} \tag{S16}$$

$${R_1}^2 = x^2 + (z+\frac{w}{2}-\sqrt{\frac{w^2}{4}-x^2})^2$$

Similarly, for the concaved surface,

$$E_{z,concave} = \frac{\sigma L}{\pi\varepsilon_0}\int_0^{w/2} \frac{(z-\frac{w}{2}+\sqrt{\frac{w^2}{4}-x^2})}{{R_2}^2\sqrt{4{R_2}^2+L^2}}dx \quad \text{, where} \tag{S17}$$

$${R_2}^2 = x^2 + \left(z-\frac{w}{2}+\sqrt{\frac{w^2}{4}-x^2}\right)^2$$

For the numerical simulations, L=50 mm, W=32 mm, and σ=3 μC/m^2 were used.

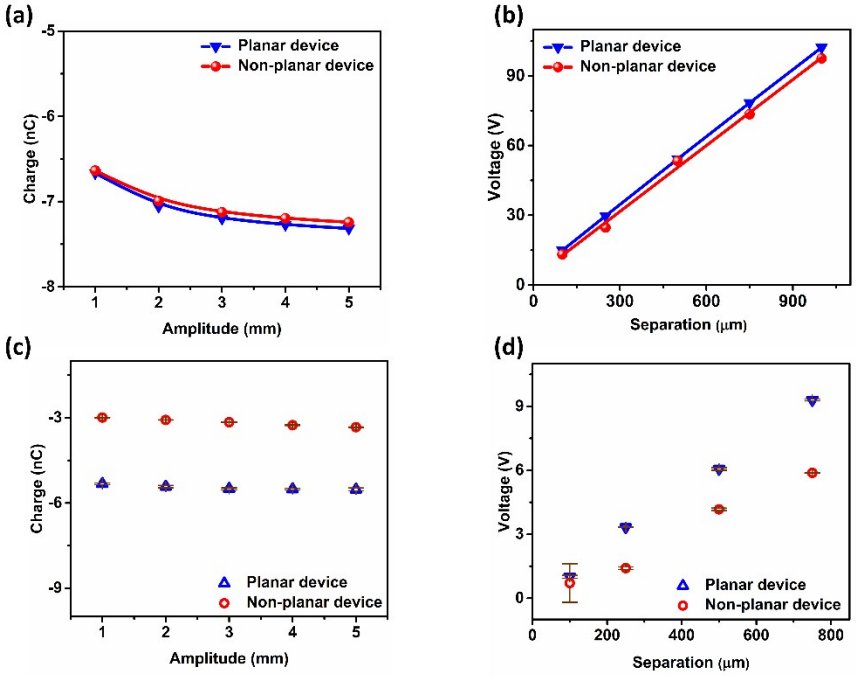

Figure S.14 Output comparison between planar and non-planar devices

Fig. S.14: Simulated output using the distance-dependent model for (a) Output charge at increasing amplitudes (H=1 mm), and, (b) V_{OC} *at different TENG layer separations. (c)-(d) Comparable experimental outputs. Error bars indicate standard deviation of 10 readings.*

Supplementary References:

1 M. Abramowitz and I. A. Stegun, *Handbook of mathematical functions: with formulas, graphs, and mathematical tables*, Courier Corporation, 1964, vol. 55.

2 W. Tang, B. Meng and H. X. Zhang, *Nano Energy*, 2013, **2**, 1164–1171.

3 S. Niu, S. Wang, L. Lin, Y. Liu, Y. S. Zhou, Y. Hu and Z. L. Wang, *Energy Environ. Sci.*, 2013, **6**, 3576.